

## Article

# Study on Restoring Force Model of Cold-Formed Thin-Walled Steel Lipped Channel Beam-Columns under Cyclic Load

Xingyou Yao <sup>1,2,\*</sup> , Jiabao Yang <sup>1</sup> and Yanli Guo <sup>1</sup><sup>1</sup> School of Civil and Architectural Engineer, Nanchang Institute of Technology, Nanchang 330099, China<sup>2</sup> Jiangxi Province Key Laboratory of Hydraulic & Civil Engineering Infrastructure Security, Nanchang 330099, China

\* Correspondence: yaoxingyoujd@163.com; Tel.: +86-150-7919-0103

**Abstract:** In order to study the hysteretic behavior and restoring force model of cold-formed thin-walled steel (CFTWS) lipped channel beam-column, a finite element analysis (FEA) model considering the material and geometric nonlinearity and the influence of the initial geometric imperfection under cyclic loading was established by ABAQUS software. Based on the verified FEA model, the hysteretic behavior of CFTWS lipped channel beam-column members with different influencing factors was analyzed by parameterization. The effects of width-to-thickness ratio, axial compression ratio and slenderness ratio on ductility, energy dissipation capacity and stiffness degradation were studied. Based on the results of parameter analysis and the theoretical and regression analysis, the calculation formula of each characteristic point of the trilinear skeleton curve of beam-column member was proposed. Based on the hysteresis curve analysis of beam-column member, the simplified restoring force model (SRFM) of CFTWS lipped channel beam-column was established according to different hysteresis rules for the different buckling modes. The results showed that the SRFM under different buckling modes was in good agreement with the hysteretic curve of FEA, which can better indicate the hysteretic behavior of the member. The proposed SRFM was accurate and applicable, and can provide a fundament for the seismic analysis of the CFTWS lipped channel beam-column.

**Keywords:** cold-formed thin-walled steel; beam-column; finite element analysis; hysteretic behavior; skeleton curve; restoring force model



**Citation:** Yao, X.; Yang, J.; Guo, Y. Study on Restoring Force Model of Cold-Formed Thin-Walled Steel Lipped Channel Beam-Columns under Cyclic Load. *Buildings* **2023**, *13*, 114. <https://doi.org/10.3390/buildings13010114>

Academic Editor: André Rafael Dias Martins

Received: 15 December 2022

Revised: 26 December 2022

Accepted: 29 December 2022

Published: 1 January 2023



**Copyright:** © 2023 by the authors. Licensee MDPI, Basel, Switzerland. This article is an open access article distributed under the terms and conditions of the Creative Commons Attribution (CC BY) license (<https://creativecommons.org/licenses/by/4.0/>).

## 1. Introduction

Cold-formed thin-walled steel has the advantages of being light-weight and high-strength, environmentally protected, industrially produced, easy to assemble, having good seismic performance and sufficient safety reserve. At the same time, due to the complex buckling modes of CFTWS, its hysteretic behavior is greatly affected. The rapid development of CFTWS leads the development of steel structure building. In recent years especially, the fabricated CFTWS low and multi-story CFTWS buildings have increased rapidly. With the popularization of low and multi-story CFTWS buildings, it is essential to study the seismic performance of CFTWS members with potential for development and optimization [1,2].

Kumar et al. [3] analyzed the response of CFTWS structures under seismic action. The concept of damage index was used to explain the degradation of strength and stiffness of structures under cyclic loads and to give a more accurate description of the impact of box section columns on the hysteretic behavior of the entire member due to local buckling of the plate. Usami et al. [4] conducted numerical research on CFTWS rectangular and tube hollow columns under the constant axial force and the horizontal cyclic load on the top of the column. Then, a simplified calculation formula of the bearing capacity and ductility for various types of members was proposed by studying the stress mechanism, bearing capacity and ductility. Goggins et al. [5,6] conducted experimental studies on the response

of CFTWS pipe members under monotonous axial loading and cyclic axial loading. The study results indicated that the strength and ductility of the specimen were significantly degraded after local buckling. The larger the slenderness ratio of the specimen, the weaker the energy dissipation capacity. Yang et al. [7] conducted experiments and numerical studies on the hysteretic behavior of cold-formed steel columns with hollow rectangular section. The results show that local buckling is the main factor causing the energy dissipation of the specimen, and the suitable axial compression ratio and slenderness ratio can greatly improve the ductility of the specimen and ensure the full use of the energy consumption capacity of plastic development. David et al. [8,9] conducted hysteretic behavior tests on C-type axial members and flexural members of cold-formed thin-wall steel. The results indicated that the different buckling modes were the key factors affecting the reduction of maximum bearing capacity, stiffness degradation and energy dissipation of the members. Li et al. [10] conducted experimental studies on CFTWS under cyclic axial loading. The study results indicated that the slenderness ratio and the width-to-thickness ratio had a significant impact on the hysteretic behavior and failure mode of the specimen. Therefore, a design suggestion was proposed to limit the width-to-thickness ratio and the slenderness ratio. Jiang et al. [11] studied the hysteretic behavior of CFTWS tube beam-columns under cyclic load. Theoretical analysis used the nonlinear multi-spring model, and the theoretical results are compared with the analysis results of the finite element shell model under the seismic response at the two-dimensional level. The results showed that the nonlinear multi-spring model can accurately simulate the hysteretic behavior of CFTWS tube beam-columns.

In recent years, some researchers have studied the SRFM of members. Wen et al. [12,13] conducted experimental research on the hysteretic behavior of the thick-walled hollow section beam-columns. The research results indicated that the axial compression ratio, the slenderness ratio and the width-to-thickness ratio are the three main parameters affecting the hysteretic behavior of the beam-column member. A SRFM which can reflect the hysteretic behavior of the member under different buckling modes is proposed. Fu et al. [14,15] conducted experimental studies on the hysteretic behavior of cold-formed thick-walled steel lipped channel beam-columns members. The study showed that the axial compression ratio, the slenderness ratio and the width-to-thickness ratio had different effects on the characteristic points of the skeleton curve of the member. Through regression calculation and analysis, the SRFM of the members under different buckling modes are established. Chen et al. [16] conducted numerical research on SRFM of uniaxial bending of the H-section member considering local buckling. A SRFM considering the degradation caused by the local buckling correlation of the plate is proposed. Yang et al. [17,18] conducted experiments and FEA on the hysteretic behavior of cold-formed thin-walled C-shaped steel column. A SRFM is proposed based on the unique double stiffness criterion of thin-walled members. At present, the research of many scholars on SRFM mainly focuses on reinforced concrete structures, composite shear walls and steel frame structures [19–31], while the research on the SRFM of CFTWS members is relatively small. The research on the SRFM of a member considering the hysteretic behavior of the member under different buckling modes under cyclic load is not sufficient; therefore, it is necessary to study the SRFM and the hysteretic behavior of the CFTWS lipped channel beam-columns in different failure modes.

Thus this paper uses the ABAQUS software to establish a FEA model of the CFTWS lipped channel beam-column member, which is used to analyze the influence of different influencing factors on its hysteretic behavior. Based on the results of the parametric analysis, a SRFM of the CFTWS lipped channel beam-column member with different hysteresis rules is established considering the hysteretic behavior of the different buckling modes, which provides a theoretical basis for studying the seismic design of the CFTWS structure.

## 2. Establishment and Verification of FEA Models

### 2.1. Establishment of FEA Model

The member nomenclature of the CFTWS lipped channel beam-column is explained in Figure 1. As shown in Figure 2, a FEA model of CFTWS lipped channel beam-column member is established using the ABAQUS software. S9R5 thin-shell element is used. The material and geometric nonlinear are considered. The bottom end of the member constrains all degrees of freedom. The top end constrains other degrees of freedom except for translation in the  $y$  and  $z$  directions, and applies an axial compressive load  $N$  in the  $z$  direction and a repeated horizontal cyclic load  $V$  in the  $y$  direction at the top end centroid. The global buckling imperfection takes the  $L/750$  of the member length, and the initial imperfection of the local imperfection takes the first-order buckling mode of the member.  $L$  represents the effective length of the member.

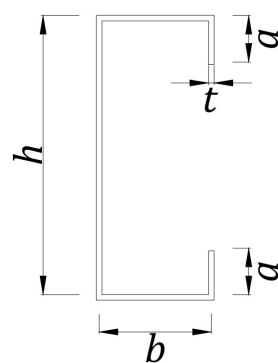


Figure 1. Definition of symbols.

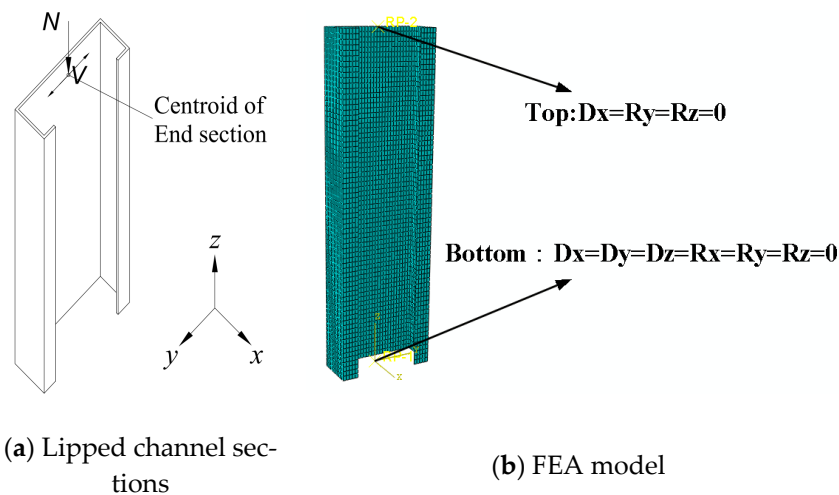


Figure 2. FEA model diagram. (a) Lipped channel sections, (b) FEA model.

The ideal elastic-plastic model is adopted for the CFTWS lipped channel beam-column members. The material properties of the FEA models are that the elastic modulus  $E$  is 206,000 MPa, the Poisson  $\mu$  is 0.3, the yield strength  $f_y$  and the tensile strength  $f_u$  were 345 MPa and 450 MPa, respectively.

The FEA model loading protocol [15] is shown in Figure 3.  $\delta_y$  is the estimated yielding displacement evaluated from the monotonic tensile tests of the material.  $\delta$  is the horizontal displacement at the column top. The yield displacement  $\delta_y$  calculated by Equation (1):

$$\delta_y = \frac{2(1-n)\sigma_y L^2}{3Eh} \quad (1)$$

where:  $n$  ( $n = N/f_y A$ ,  $A$  = area of column member) indicates the axis compression ratio of the member,  $E$  is the elastic modulus of the member,  $h$  represents the web height of the member.

Since the CFTWS has a large deformation after buckling and the bearing capacity declines rapidly and in order to analyze the whole process after its buckling and peak load, in the process of applying horizontal reciprocating displacement to the top end of the member, the loading control is divided into two stages of elasticity and buckling. The elastic stage is one cycle of displacement per stage; each stage is  $\pm 0.25\delta_y$ ,  $\pm 0.5\delta_y$ ,  $\pm 0.75\delta_y$ . After buckling, each stage is cycled three times; each stage is  $\pm\delta_y$ ,  $\pm 1.5\delta_y$ ,  $\pm 2\delta_y$ ,  $\pm 2.5\delta_y$ ,  $\pm 3\delta_y$  . . . The loading process runs until the member is destroyed or seriously deformed.

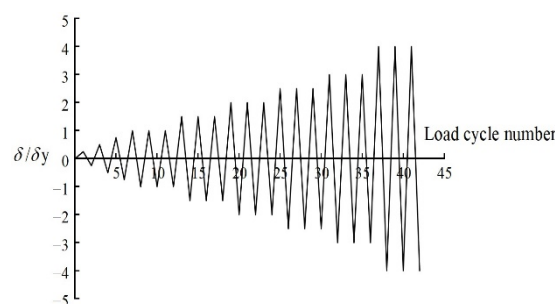


**Figure 3.** Loading protocol.

## 2.2. Verification on FEA Model

The established FEA model was used to simulate the specimens C1-BC-L30-70-02 and C2-BC-L60-35-02 [7]. The material properties of specimens are shown in Table 1. The test specimens were labeled as “C-BC- $\lambda$ - $h/t$ - $n$ ”, where “C” meant lipped channel section, “BC” meant the loading mode is cyclic loading of beam-column member, “ $\lambda$ ” represented the slenderness ratio, “ $h/t$ ” represented the ratio of the width-to-thickness, “ $n$ ” represented the axis compression ratio of the member. The yield strength is 291.0 MPa and 270.3 MPa for specimens C1-BC-L30-70-02 and C2-BC-L60-35-02, respectively. Figure 4 shows the hysteresis curves of each specimen. Figure 5 shows the failure mode of each specimen.

**Table 1.** Material properties.

Specimen	$h$ (mm)	$b$ (mm)	$a$ (mm)	$t$ (mm)	$L$ (mm)	$n$
C1-BC-L30-70-02	199.4	69.9	19.3	2.85	1277	0.2
C2-BC-L60-35-02	251.3	79.6	49.7	7.43	2945	0.2

From Figure 4, it can be seen that the hysteresis curve obtained by the FEA is relatively consistent with the test hysteresis curve in terms of peak force. The shape and fullness of hysteresis curves obtained by FEA are consistent with those obtained by test. As can be seen from Figure 5, the failure mode form obtained by FEA is basically consistent with the failure mode obtained by test. As shown in Figure 5a, FEA and test results show that the failure mode of C1-BC-L30-70-02 member is manifested as local bulging of the web at column foot and flange cohesion. As shown in Figure 5b, FEA and test results show that the failure mode of C2-BC-L60-35-02 member is the column foot concaving in the web and the slightly expanded flange. The comparison shows that the FEA model developed in this paper can be used to analyze the hysteretic behavior of CFTWS lipped channel beam-column members under the cyclic load.

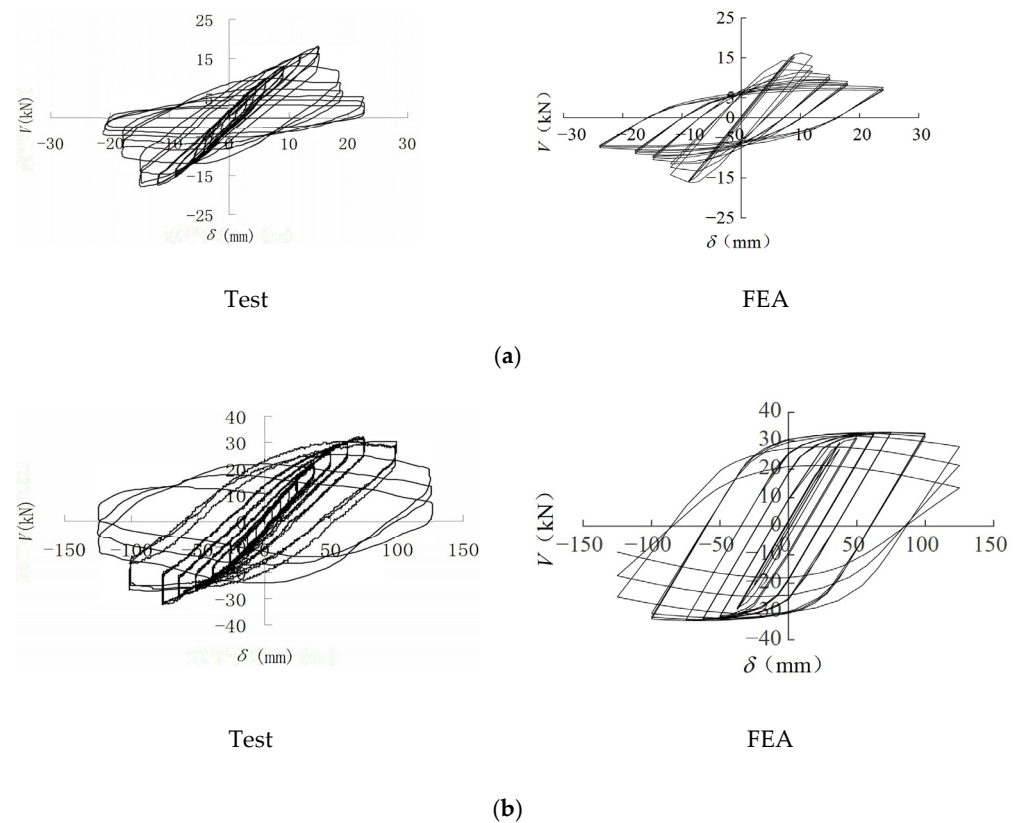


**Figure 4.** Comparison on hysteresis curves between test and FEA. (a) Hysteresis curve of C1-BC-L30-70-02; (b) Hysteresis curve of C2-BC-L60-35-02.

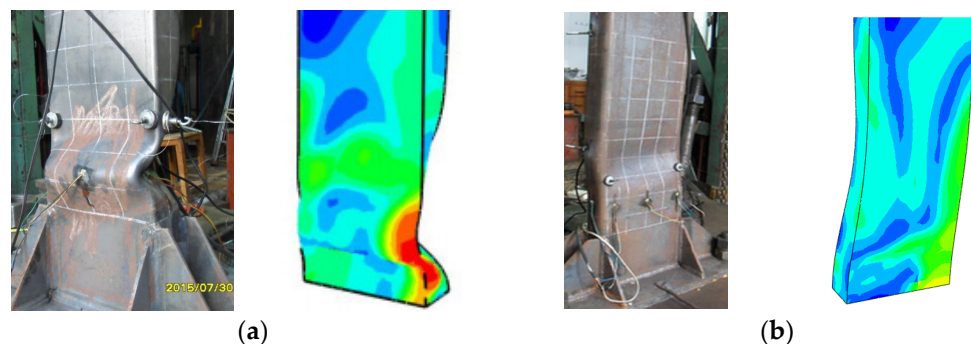


**Figure 5.** Comparison on failure mode between test and FEA. (a) Failure mode of C1-BC-L30-70-02; (b) Failure mode of C2-BC-L60-35-02.

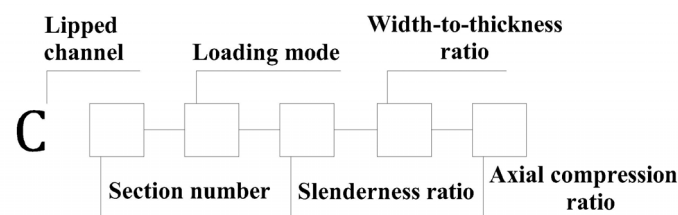
### 3. Parameter Analysis of Hysteretic Behavior

#### 3.1. Member Design

Through the parametric analysis of the hysteretic behavior of 80 CFTWS lipped channel beam-column members, the influence of the slenderness ratio, the axial compression ratio and the width-to-thickness ratio on the hysteretic behavior of the CFTWS lipped channel member was determined. The selected CFTWS lipped channel sections are shown in Table 2. The specific symbol of CFTWS lipped channel section is shown in Figure 6. For example, the member C2-BC-L50-50-03 means as follows: BC indicates the horizontal cyclic load and the constant axial force under the top of column, L50 represents that the slenderness ratio ( $\lambda$ ) about the weak axis is 50, 50 means that the ratio of the width-to-thickness ( $h/t$ ) is 50, 03 indicates that the axial compression ratio ( $n$ ) is 0.3.

**Table 2.** Cold-formed thin-wall steel lipped channel beam-column sections for FEA.

Members	$h \times b \times a \times t \times L$ (mm)	Analysis Parameters			
		$h/t$	$\lambda$	$n$	$f_y$ (MPa)
C1-BC-L15-40-00	120 × 48 × 20 × 3 × 385	40	15	0.0(0.1, 0.2, 0.3, 0.4)	345
C1-BC-L30-40-00	120 × 48 × 20 × 3 × 770	40	30	0.0(0.1, 0.2, 0.3, 0.4)	345
C1-BC-L50-40-00	120 × 48 × 20 × 3 × 1280	40	50	0.0(0.1, 0.2, 0.3, 0.4)	345
C1-BC-L70-40-00	120 × 48 × 20 × 3 × 1800	40	70	0.0(0.1, 0.2, 0.3, 0.4)	345
C2-BC-L15-50-00	150 × 60 × 25 × 3 × 500	50	15	0.0(0.1, 0.2, 0.3, 0.4)	345
C2-BC-L30-50-00	150 × 60 × 25 × 3 × 1000	50	30	0.0(0.1, 0.2, 0.3, 0.4)	345
C2-BC-L50-50-00	150 × 60 × 25 × 3 × 1680	50	50	0.0(0.1, 0.2, 0.3, 0.4)	345
C2-BC-L70-50-00	150 × 60 × 25 × 3 × 2350	50	70	0.0(0.1, 0.2, 0.3, 0.4)	345
C3-BC-L15-60-00	180 × 72 × 30 × 3 × 630	60	15	0.0(0.1, 0.2, 0.3, 0.4)	345
C3-BC-L30-60-00	180 × 72 × 30 × 3 × 1250	60	30	0.0(0.1, 0.2, 0.3, 0.4)	345
C3-BC-L50-60-00	180 × 72 × 30 × 3 × 2100	60	50	0.0(0.1, 0.2, 0.3, 0.4)	345
C3-BC-L70-60-00	180 × 72 × 30 × 3 × 2935	60	70	0.0(0.1, 0.2, 0.3, 0.4)	345
C4-BC-L15-70-00	210 × 84 × 35 × 3 × 760	70	15	0.0(0.1, 0.2, 0.3, 0.4)	345
C4-BC-L30-70-00	210 × 84 × 35 × 3 × 1525	70	30	0.0(0.1, 0.2, 0.3, 0.4)	345
C4-BC-L50-70-00	210 × 84 × 35 × 3 × 2550	70	50	0.0(0.1, 0.2, 0.3, 0.4)	345
C4-BC-L70-70-00	210 × 84 × 35 × 3 × 3560	70	70	0.0(0.1, 0.2, 0.3, 0.4)	345

**Figure 6.** Notation of lipped channel section.

### 3.2. Parameter Analysis

The variable parameter analysis on the hysteretic behavior for the CFTWS lipped channel beam-column members were conducted by FEA. The effects of the axial compression ratio, the width-to-thickness ratio and the slenderness ratio on the failure mode, bearing capacity, ductility ratio, energy dissipation and the stiffness degradation of the CFTWS lipped channel beam-column members were investigated.

#### 3.2.1. Failure Mode

The failure mode analyzed by FEA for members C4-BC-L15-70-02, C3-BC-L30-60-03 and C1-BC-L70-40-02 is shown in Figure 7, exhibiting local buckling, distortional buckling and global buckling, respectively. The failure modes of all CFTWS lipped channel beam-column members show that the short columns and medium columns with large width-to-thickness ratios are easy to be local buckling, the distortional buckling can be found for the medium columns with a small width ratio of flange to lip, and the long columns with a small width-to-thickness ratio fail with global buckling.

It can be seen from Figure 8 that the member C4-BC-L15-70-02 still has a considerable post-buckling strength. The shape of the hysteresis curve is full, which indicates that the member that has local buckling failure has a good energy consumption capacity. The bearing capacity of the member slowly decreases with the increase of the loading stage, which indicates that the stiffness degradation is slower. The C3-BC-L30-60-03 hysteresis curve of the member is relatively full, and still has a large bearing capacity after the member is buckled, indicating that the member with distortional buckling failure can still maintain good hysteretic behavior. The C1-BC-L70-40-02 hysteresis curve is not relatively full, and the stiffness degrades quickly. With the increase of the loading stage, the bearing capacity of the member declines rapidly. This indicates that the global buckling of the member hysteretic behavior is poor, and this buckling mode should be avoided in practical engineering.

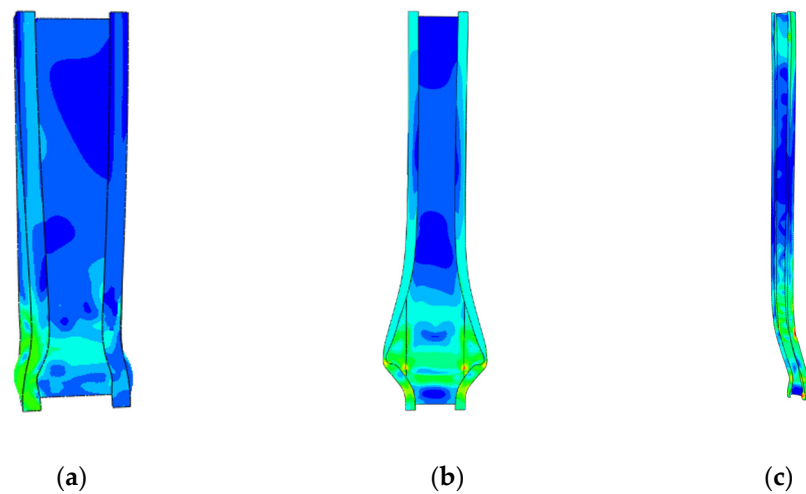


**Figure 7.** Failure modes. (a) Local buckling of C4-BC-L15-70-02; (b) Distortional buckling of C3-BC-L30-60-03; (c) Global buckling of C1-BC-L70-40-02.

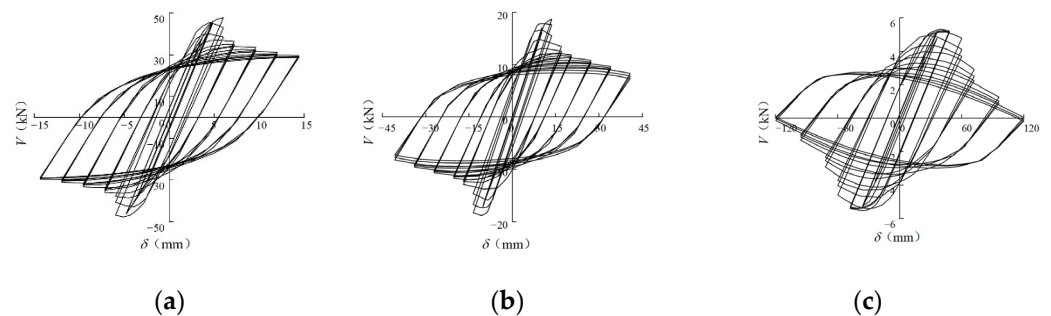


**Figure 8.** Hysteresis curves. (a) Hysteresis curves of C4-BC-L15-70-02; (b) Hysteresis curves of C3-BC-L30-60-03; (c) Hysteresis curves of C1-BC-L70-40-02.

### 3.2.2. Skeleton Curve

The skeleton curve is expressed by the relation between  $M/M_p$  and the relative angle ( $\varphi$ ) of the member.  $M$  is the plastic bending moment of the member, and it is obtained by the FEA.  $M_p$  represents the plastic moment of the full section of the member. The relative angle is  $\varphi = \delta/L(\%)$ ,  $\delta$  is the horizontal displacement at the column top, and  $L$  represents the effective length of the member. Through the analysis of the dimensionless skeleton curve of the member, the influence of the slenderness ratio, the axial compression ratio and the width-to-thickness ratio on its initial stiffness, peak load, ductility and the stiffness degradation is reflected from the rotational ability and plasticity development degree of the member.

#### 1. The slenderness ratio

FEA yields the skeleton curve pair of the CFTWS lipped channel beam-column member with different slenderness ratios, as shown in Figure 9 (limited to the length of the skeleton curve change of only some members).

As can be seen from Figure 9, the plastic bending moment and initial elastic stiffness of the member decrease with the increase of the slenderness ratio when rotating at the same angle. The bearing capacity and the initial stiffness of the member decreases with the increase of the slenderness ratio. The stiffness degradation of the member is accelerated with the increase of slenderness ratio.

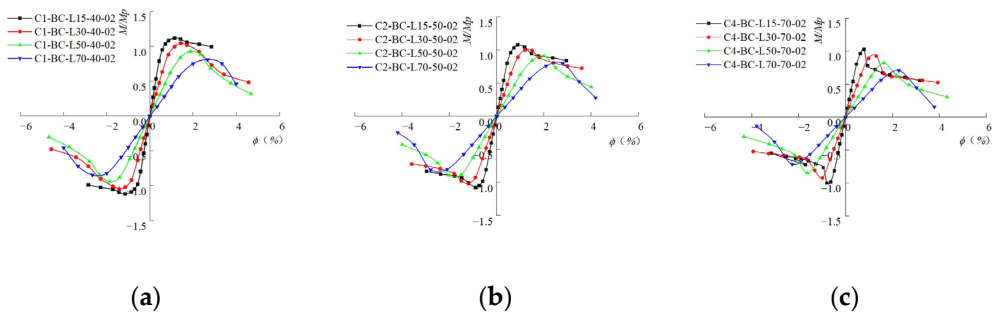


**Figure 9.** The slenderness ratio effect. (a)  $h/t = 40$ ,  $n = 0.2$ ; (b)  $h/t = 50$ ,  $n = 0.2$ ; (c)  $h/t = 70$ ,  $n = 0.2$ .

## 2. The width-to-thickness ratio

Figure 10 shows the comparison of skeleton curves of the CFTWS lipped channel beam-column members with different width-to-thickness ratios.

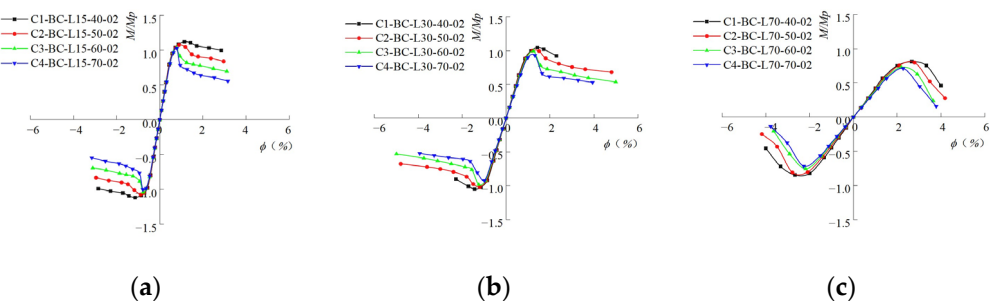


**Figure 10.** The effect of width-to-thickness ratio. (a)  $\lambda = 15$ ,  $n = 0.2$ ; (b)  $\lambda = 30$ ,  $n = 0.2$ ; (c)  $\lambda = 70$ ,  $n = 0.2$ .

From Figure 10, it can be seen that the skeleton curves of members with different width-to-thickness ratios almost coincide when the plates have not yet yielded in the elastic stage. In the yield stage of member, the plastic bending moment and rotation capacity of the member decrease with the increase of width-to-thickness ratio. The stiffness degradation of members accelerates after reaching the ultimate bearing capacity.

## 3. Axial compression ratio

Figure 11 shows the comparison of the skeleton curves of the CFTWS lipped channel beam-column member when the axial compression ratio of the same member changes.

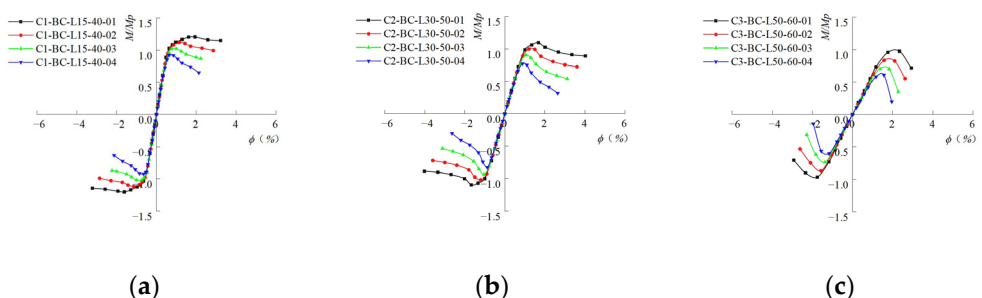


**Figure 11.** The effect of axial compression ratio. (a)  $\lambda = 15$ ,  $h/t = 40$ ; (b)  $\lambda = 30$ ,  $h/t = 50$ ; (c)  $\lambda = 50$ ,  $h/t = 60$ .

From Figure 11, it can be seen that the initial stiffness of the skeleton curve is similar at the beginning of loading. Due to the different static axial forces, the position of the peak point and the later rotation capacity of the four members are quite different. This shows the plastic bending moment and ductility of the member decrease with the increase of axial compression ratio.

### 3.2.3. Analysis of Hysteretic Behavior of Beam-Column Member

#### 1. Ductility

Ductility is a mechanical property to measure the plastic deformation ability of a member. The displacement ductility coefficient  $\mu$  is used to describe the ductility performance of the member. The calculation formula is:

$$\mu = \delta_u / \delta_y \quad (2)$$

where  $\delta_u$  is the ultimate displacement corresponding to the displacement; when the horizontal force decreases to 85% of the peak load,  $\delta_y$  is the yield displacement of the member.

As shown in Table 3, the ductility coefficient of most members is stable between 1 and 2. When the width-to-thickness ratio has a more significant effect on  $\mu$ , the displacement ductility coefficient of the member decreases with the increase of width-to-thickness ratio. This is mainly because the web of the member with larger width is more prone to buckling, which leads to the decrease of its deformation ability and the ductility.

**Table 3.** Ductility coefficients of members.

Members	$\mu$	Members	$\mu$	Members	$\mu$	Members	$\mu$
C1-BC-L15-40-01	1.77	C1-BC-L30-40-01	1.66	C1-BC-L50-40-01	1.67	C1-BC-L70-40-01	1.63
C1-BC-L15-40-02	1.68	C1-BC-L30-40-02	1.40	C1-BC-L50-40-02	1.45	C1-BC-L70-40-02	1.40
C1-BC-L15-40-03	1.67	C1-BC-L30-40-03	1.47	C1-BC-L50-40-03	1.36	C1-BC-L70-40-03	1.30
C1-BC-L15-40-04	1.67	C1-BC-L30-40-04	1.47	C1-BC-L50-40-04	1.35	C1-BC-L70-40-04	1.33
C2-BC-L15-50-01	1.80	C2-BC-L30-50-01	1.42	C2-BC-L50-50-01	1.47	C2-BC-L70-50-01	1.43
C2-BC-L15-50-02	1.58	C2-BC-L30-50-02	1.56	C2-BC-L50-50-02	1.38	C2-BC-L70-50-02	1.35
C2-BC-L15-50-03	1.61	C2-BC-L30-50-03	1.47	C2-BC-L50-50-03	1.35	C2-BC-L70-50-03	1.30
C2-BC-L15-50-04	1.62	C2-BC-L30-50-04	1.47	C2-BC-L50-50-04	1.33	C2-BC-L70-50-04	1.29
C3-BC-L15-60-01	1.63	C3-BC-L30-60-01	1.65	C3-BC-L50-60-01	1.51	C3-BC-L70-60-01	1.49
C3-BC-L15-60-02	1.43	C3-BC-L30-60-02	1.33	C3-BC-L50-60-02	1.53	C3-BC-L70-60-02	1.47
C3-BC-L15-60-03	1.37	C3-BC-L30-60-03	1.27	C3-BC-L50-60-03	1.42	C3-BC-L70-60-03	1.17
C3-BC-L15-60-04	1.36	C3-BC-L30-60-04	1.28	C3-BC-L50-60-04	1.38	C3-BC-L70-60-04	1.25
C4-BC-L15-70-01	1.48	C4-BC-L30-70-01	1.41	C4-BC-L50-70-01	1.31	C4-BC-L70-70-01	1.29
C4-BC-L15-70-02	1.36	C4-BC-L30-70-02	1.39	C4-BC-L50-70-02	1.22	C4-BC-L70-70-02	1.25
C4-BC-L15-70-03	1.37	C4-BC-L30-70-03	1.32	C4-BC-L50-70-03	1.43	C4-BC-L70-70-03	1.24
C4-BC-L15-70-04	1.24	C4-BC-L30-70-04	1.26	C4-BC-L50-70-04	1.45	C4-BC-L70-70-04	1.22

#### 2. Energy dissipation behavior

The energy dissipation behavior of structural members can be measured by the area and shape enclosed by the hysteresis curve. Figure 12 shows the schematic diagram of hysteresis loop. In this paper, the equivalent viscous damping coefficient ( $h_e$ ) is used to measure the energy dissipation behavior of the member.  $S_{(ABC+CDA)}$  represents the energy consumed by the member in a cycle, namely the area of the ellipse in Figure 12.  $S_{(OBE+ODF)}$  represents the energy that can be absorbed by the member in a cycle, namely the area of the shaded part in Figure 12, which is calculated according to Equation (3).

$$h_e = \frac{1}{2\pi} \frac{S_{(ABC+CDA)}}{S_{(OBE+ODF)}} \quad (3)$$

The relation curve between the equivalent viscous damping coefficient ( $h_e$ ) and the load step ( $i$ th) of each member is calculated from Equation (3) and shown in Figure 13.

It can be seen from Figure 13 that the equivalent viscous damping coefficient ( $h_e$ ) of members increases with the increase of load step ( $i$ th). The greater the slenderness ratio of members, the faster  $h_e$  of members changes with  $i$ th. This means that the CFTWS lipped channel beam-column member can still maintain good energy dissipation behavior in the later stage of load step.

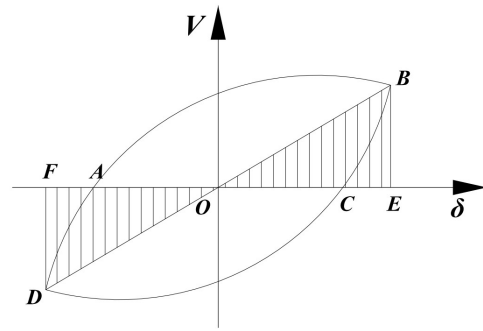


Figure 12. Schematic diagram of hysteresis loop.

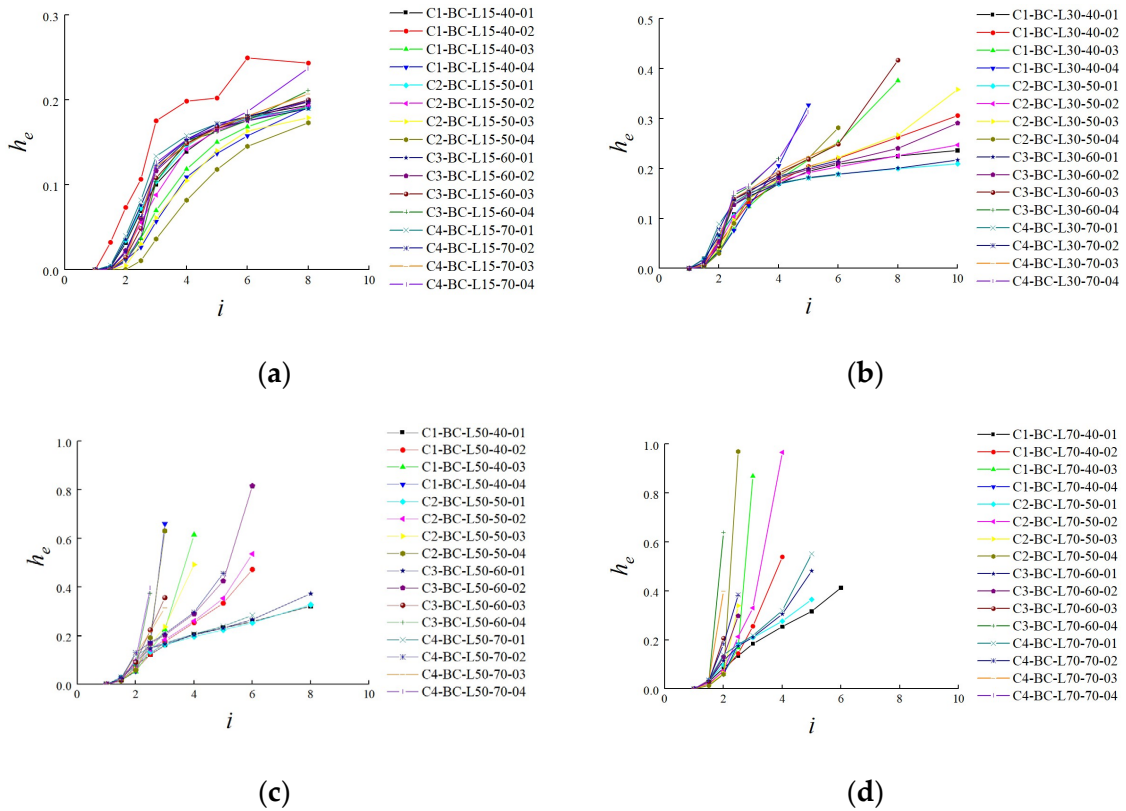


Figure 13. Relationship between equivalent viscous damping coefficients and load step. (a)  $\lambda = 15$ ; (b)  $\lambda = 30$ ; (c)  $\lambda = 50$ ; (d)  $\lambda = 70$ .

### 3. Stiffness degradation

The secant stiffness ( $K_i$ ) is used to describe the stiffness degradation. The secant stiffness should be calculated according to Equation (4):

$$K_i = \frac{|+F_i| + |-F_i|}{|+\delta_i| + |-\delta_i|} \tag{4}$$

where  $K_i$  is the secant stiffness of the  $i^{\text{th}}$  load step,  $F_i$  is the peak load value of the first cycle in the  $i^{\text{th}}$ ,  $\delta_i$  is the displacement value corresponding to the peak load value of the first cycle in the  $i^{\text{th}}$ . Figure 14 shows the relationship between  $K_i$  and  $i^{\text{th}}$ .

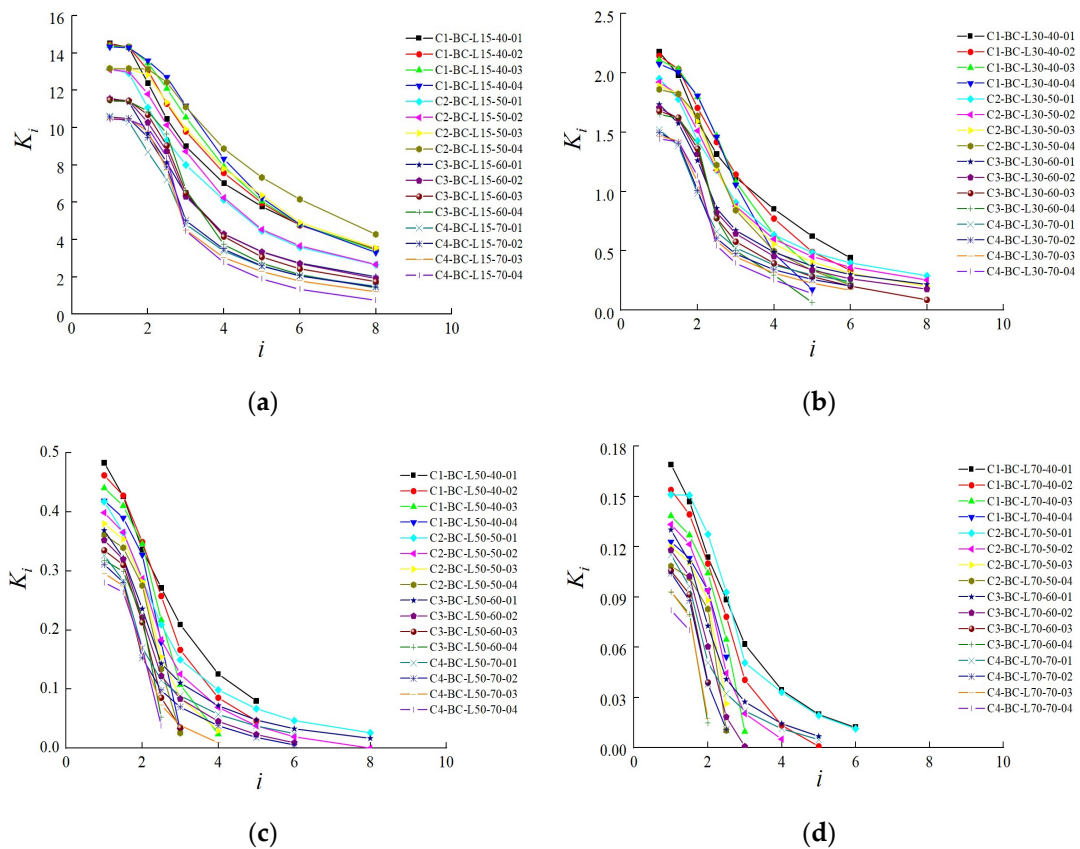


Figure 14. Relationship between  $K_i$  and  $i$ th. (a)  $\lambda = 15$ ; (b)  $\lambda = 30$ ; (c)  $\lambda = 50$ ; (d)  $\lambda = 70$ .

As shown in Figure 14, the initial secant stiffness of the member decreases with the increase of the axial compression ratio, and the degradation speed of the member stiffness increases with the increase of the axial compression ratio. The secant stiffness of the member decreases with the increase of width-to-thickness ratio or slenderness ratio.

#### 4. Simplify and Establishment of Restoring Force Model

##### 4.1. Skeleton Curve Model

The results of the FEA show that the skeleton curve of the beam-column member is basically symmetrical. As shown in Figure 15, the skeleton curve of the member can be modeled by this trilinear skeleton curve [13]. Assuming that the front and back directions of the skeleton curve are completely symmetrical, the skeleton curve model of the beam-column member is divided into three stages: OA is the elastic stage, and A is the yield load point of the member. AB is the reinforcement stage, and point B is the peak load point of the member. BC is the stiffness degradation stage, and point C is the ultimate point of the member.

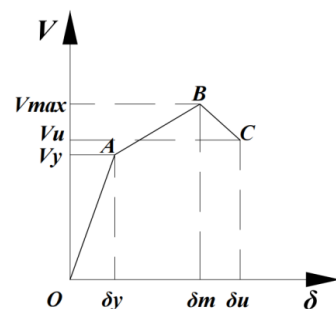


Figure 15. Definition of characteristic points of the skeleton curve.

Based on the results of FEA, the ratio between the characteristic points of the skeleton curve of the beam-column member and its three key factors of the width-to-thickness ratio ( $h/t$ ), the axial compression ratio ( $n$ ) and the slenderness ratio ( $\lambda$ ) are analyzed. The calculation formula of each characteristic point of the model is obtained by using theoretical derivation and multivariate linear fitting method. The calculation method of the characteristic points of the skeleton curve model is as follows:

1. Peak load  $V_{\max}$

In the process of solving the peak load of the member, the horizontal load  $V_{0P}$  when the beam-column member is yielded at the pure bending full-section yield is obtained according to the theoretical analysis and calculated according to Equation (5):

$$V_{0P} = \frac{M_P}{L} = \frac{f_y W_p}{L} \quad (5)$$

where  $M_p$  is the plastic bending moment when the full section of the cantilever column yields,  $W_p$  is the plastic modulus of the cantilever column section,  $L$  represents the effective length of the member,  $f_y$  is the yield strength of steel.

The maximum horizontal load  $V_{0\max}$  of the beam-column member is obtained by pure bending FEA. As shown in Figure 16,  $V_{0\max}/V_{0P}$  shows a nonlinear decreasing relationship with the increase of  $h/t$ .

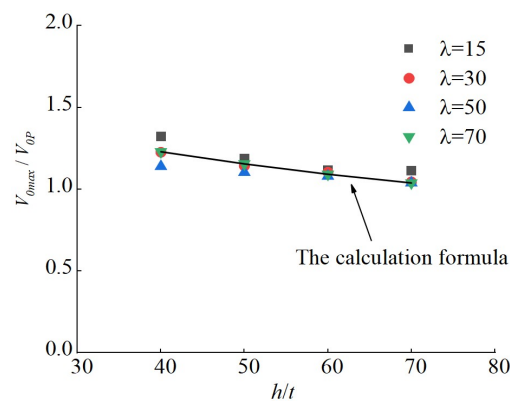


**Figure 16.** The effect of  $h/t$  on  $V_{0\max}/V_{0P}$ .

The calculation formula for obtaining  $V_{0\max}$  by regression fitting is as follows:

$$\frac{V_{0\max}}{V_{0P}} = 0.0000357 \left| \frac{h}{t} \sqrt{\frac{f_y}{235}} \right|^2 - 0.01 \frac{h}{t} \sqrt{\frac{f_y}{235}} + 1.63 \quad (6)$$

The FEA calculation results show that the peak point load  $V_{\max}$  of the member is mainly reduced by the increase of  $\lambda$  and  $n$ . As shown in Figures 17 and 18, the relationship between  $V_{\max}/V_{0\max}$  and  $n$  and  $\lambda$  is weakly nonlinear.

Multiple linear regression method was used to obtain the calculation formula of peak load, as shown in Equation (7):

$$\frac{V_{\max}}{V_{0\max}} = 1 - (a + b\lambda + c\lambda^2)n, \quad (7)$$

where  $a = 0.9673 - 1.273n$ ,  $b = -0.0191 + 0.576n$ ,  $c = 0.000327 - 0.000606n$ .

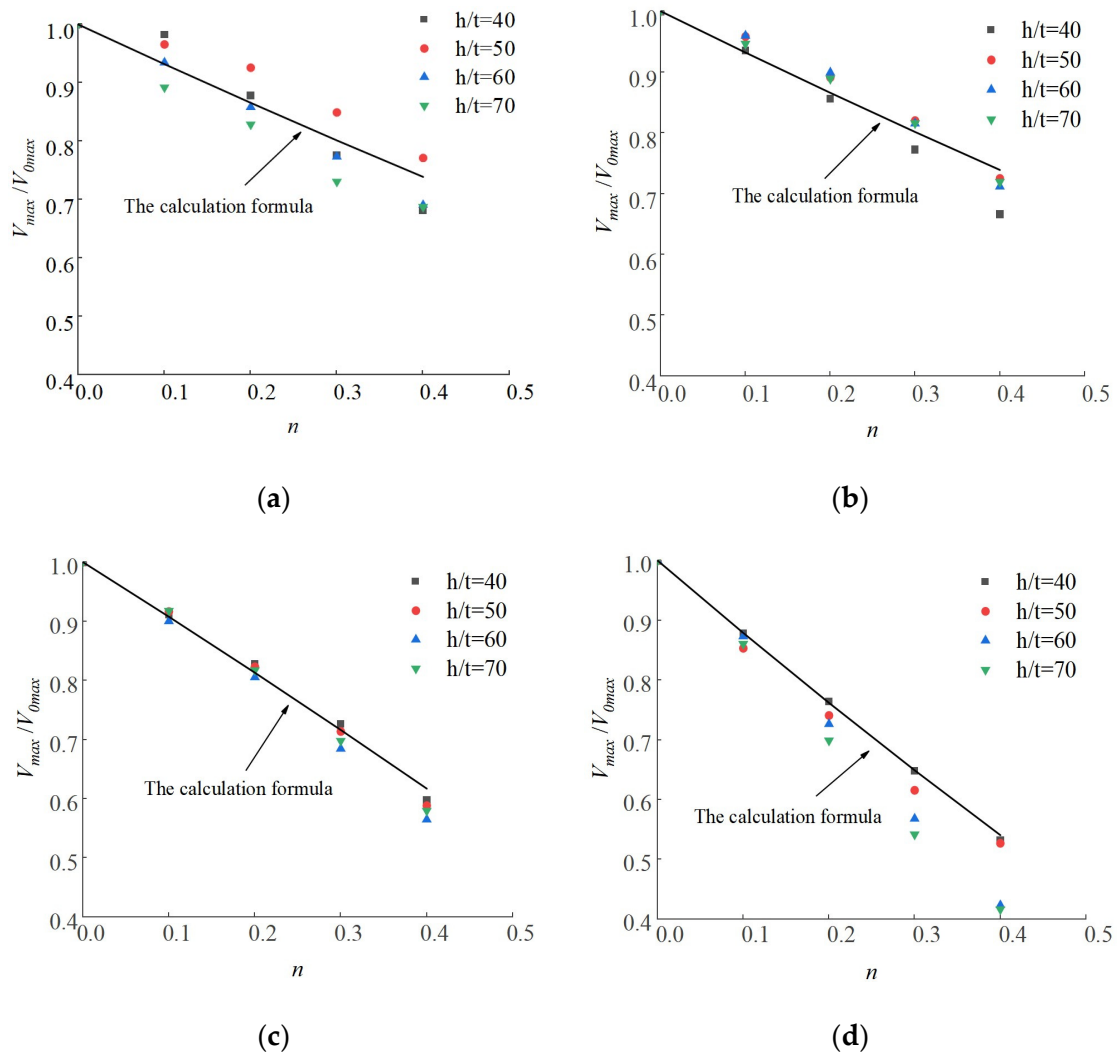


Figure 17. The effect of  $n$  on  $V_{max}/V_{0max}$ . (a)  $\lambda = 15$ ; (b)  $\lambda = 30$ ; (c)  $\lambda = 50$ ; (d)  $\lambda = 70$ .

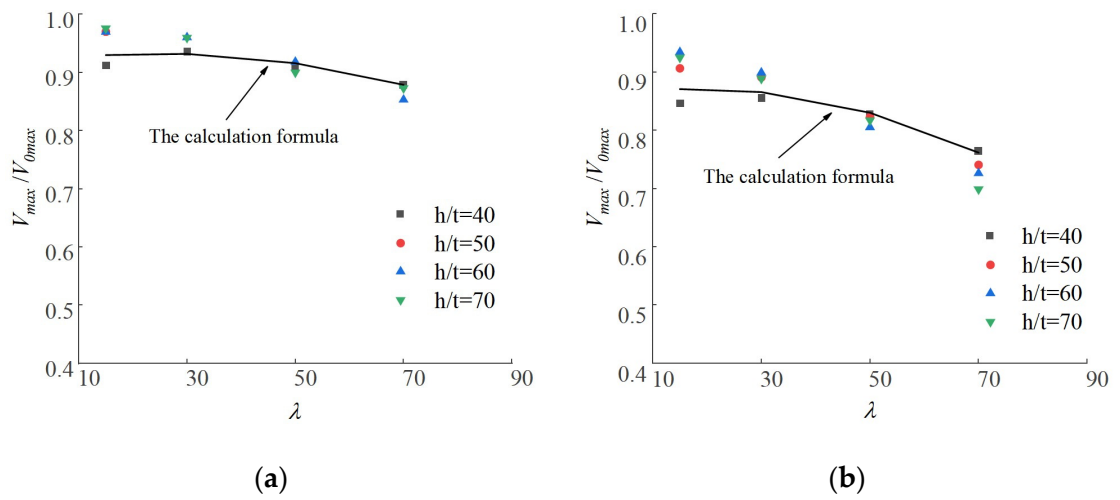


Figure 18. Cont.

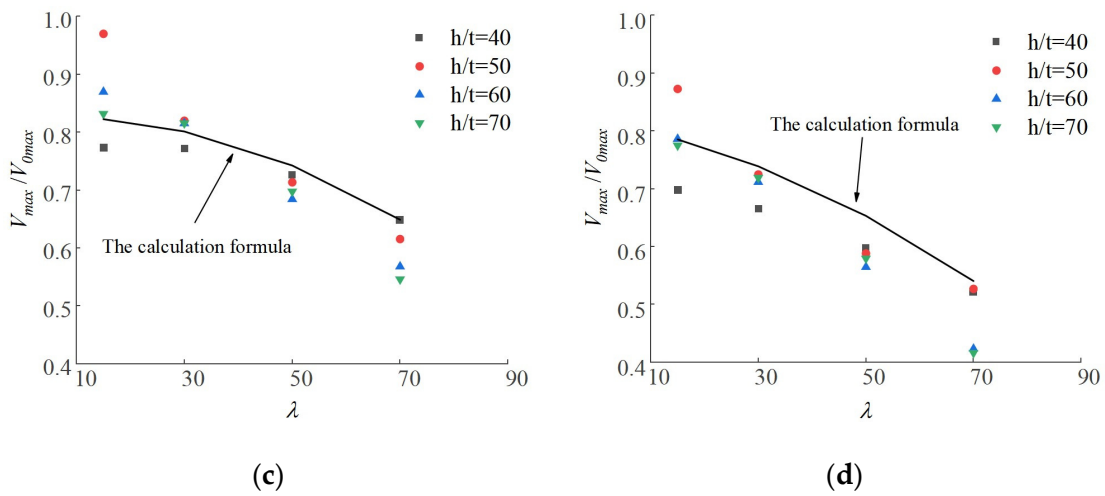


Figure 18. The effect of  $\lambda$  on  $V_{\max}/V_{0\max}$ . (a)  $n = 0.1$ ; (b)  $n = 0.2$ ; (c)  $n = 0.3$ ; (d)  $n = 0.4$ .

2. Yield load  $V_y$

As shown in Figure 19,  $V_{\max}/V_y$  has no obvious change with the slenderness ratio under the same  $n$  and the  $h/t$ . The error between the ratio range and its average value is less than about 10%, assuming that  $\lambda$  has little effect on it.

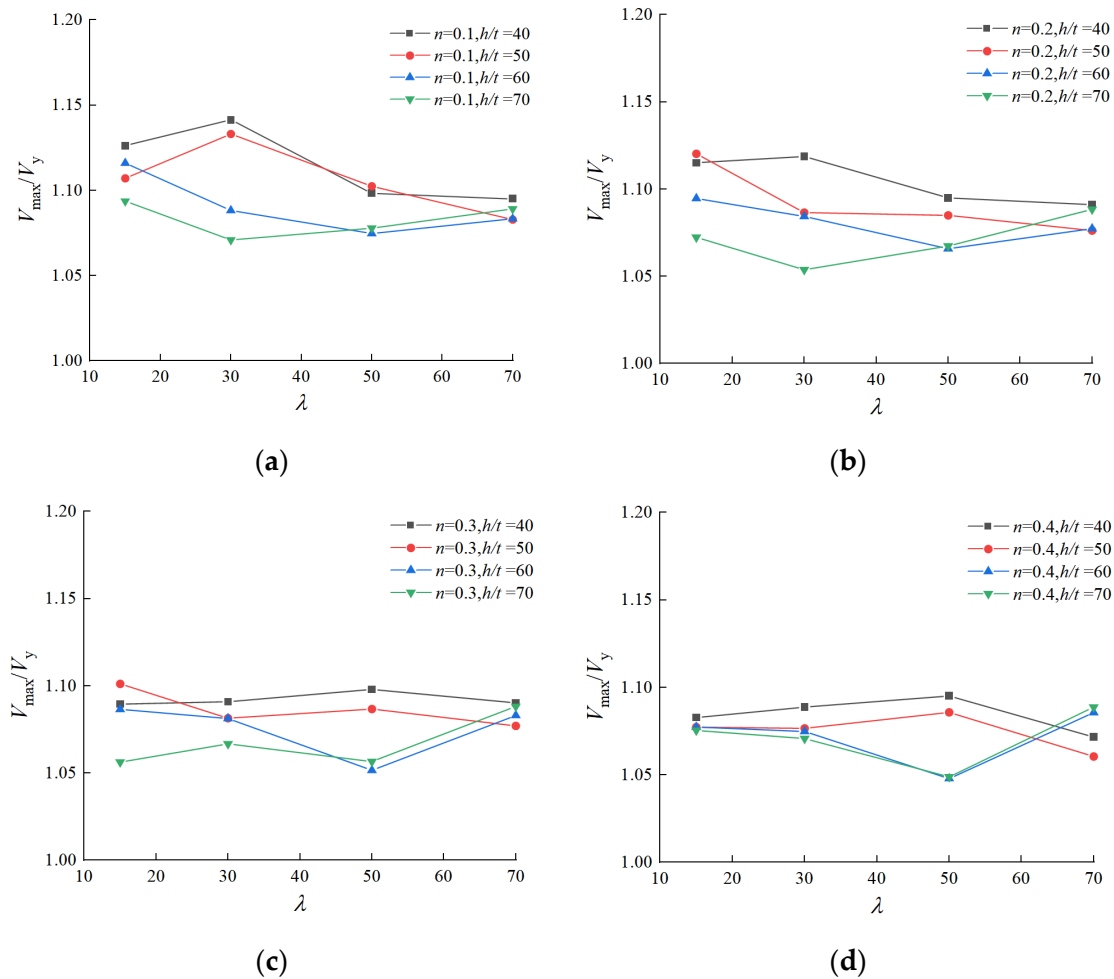


Figure 19. The effect of  $\lambda$  on  $V_{\max}/V_y$ . (a)  $n = 0.1$ ; (b)  $n = 0.2$ ; (c)  $n = 0.3$ ; (d)  $n = 0.4$ .

Through multiple regression fitting, the calculation formula of  $V_{max}/V_y$  is as follows:

$$\frac{V_{max}}{V_y} = 1.1 - 0.0765n + (0.4804 - 0.901n)n^3 \left( 3.174 - 0.2655\frac{h}{t} + 0.00784\frac{h^2}{t^2} \right) \quad (8)$$

### 3. Ultimate load $V_u$

It is assumed that the ratio of ultimate load to peak load is 0.85 as Equation (9)

$$\frac{V_u}{V_{max}} = 0.85 \quad (9)$$

### 4. Yield displacement $\delta_y$

Based on the parametric FEA results, it is found that the initial stiffness is not greatly affected by  $h/t$  and  $n$ . The theoretical calculation formula of elastic stiffness can be calculated according to the following formula. [32]

$$K = (0.65 + 0.003\lambda)K_0 \left( 1 - \frac{P}{P_E} \right) \quad (10)$$

where  $K_0 = \frac{3EI}{L^3}$ ,  $P_E = \frac{\pi^2 EI}{4L^2}$ .  $L$  is the cantilever length of the cantilever column,  $P$  is vertical axial load.

A comparison of the stiffness  $K$  obtained by the theoretical calculation formula with the initial elastic stiffness  $K_{FE}$  obtained by the FEA is shown in Figure 19. As can be seen from Figure 20,  $K/K_{FE}$  changes around 1.0, the maximum and minimum values are 1.072 and 0.912, respectively. The mean and coefficient of variation of  $K/K_{FE}$  were 1.004 and 0.028, respectively. The above results show that the initial elastic stiffness accuracy of the CFTWS lipped channel beam-column member is better in the calculation.

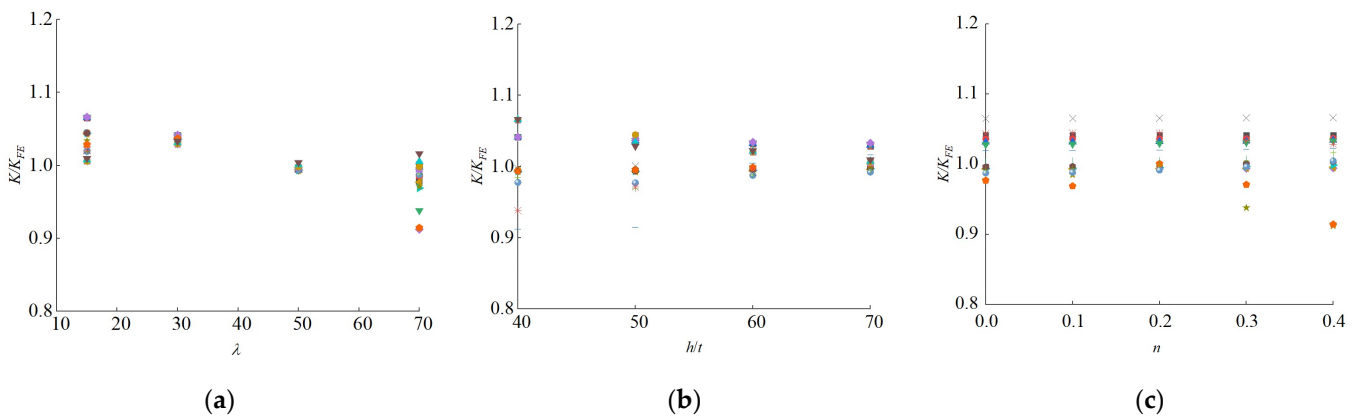


**Figure 20.** The initial elastic stiffness. (a) The effect of the  $\lambda$ ; (b) The effect of the  $h/t$ ; (c) The effect of  $n$ .

According to the linear relationship between the  $V_y$  and  $\delta_y$  in the elastic stage, the calculation formula of  $\delta_y$  can be obtained:

$$\frac{V_y}{\delta_y} = K \quad (11)$$

### 5. Peak displacement $\delta_m$

As can be seen from Figure 21, through the parametric FEA, it is found that  $\delta_m/\delta_y$  shows a nonlinear decreasing relationship with the increase of  $\lambda$  and  $h/t$ . Regression gives  $\delta_m/\delta_y$  as the formula for calculation:

$$\frac{\delta_m}{\delta_y} = 1.45 - 0.00387\lambda \tag{12}$$

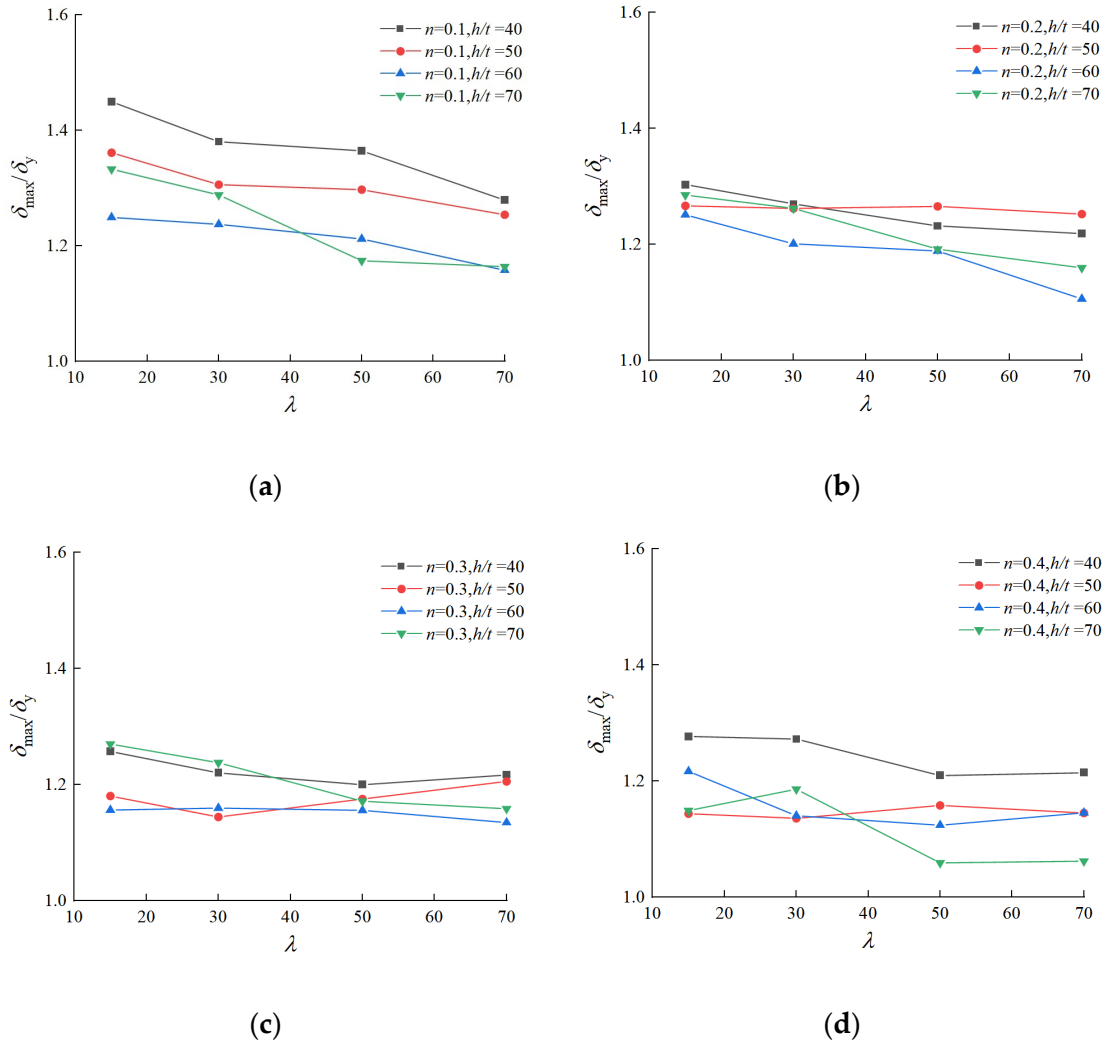


Figure 21. The effect of  $\lambda$  on  $\delta_m/\delta_y$ . (a)  $n = 0.1$ ; (b)  $n = 0.2$ ; (c)  $n = 0.3$ ; (d)  $n = 0.4$ .

### 6. Ultimate displacement $\delta_u$

As shown in Figure 22, through the analysis, it is found that  $n$  and  $h/t$  have little influence on  $\delta_u/\delta_m$ . The change of the value of  $\delta_u/\delta_m$  with  $\lambda$  did not show obvious change rule.

The value of  $\delta_u/\delta_m$  is stable at about 1.189. So the calculation formula of  $\delta_u/\delta_m$  is as follows:

$$\frac{\delta_u}{\delta_m} = 1.189 \tag{13}$$

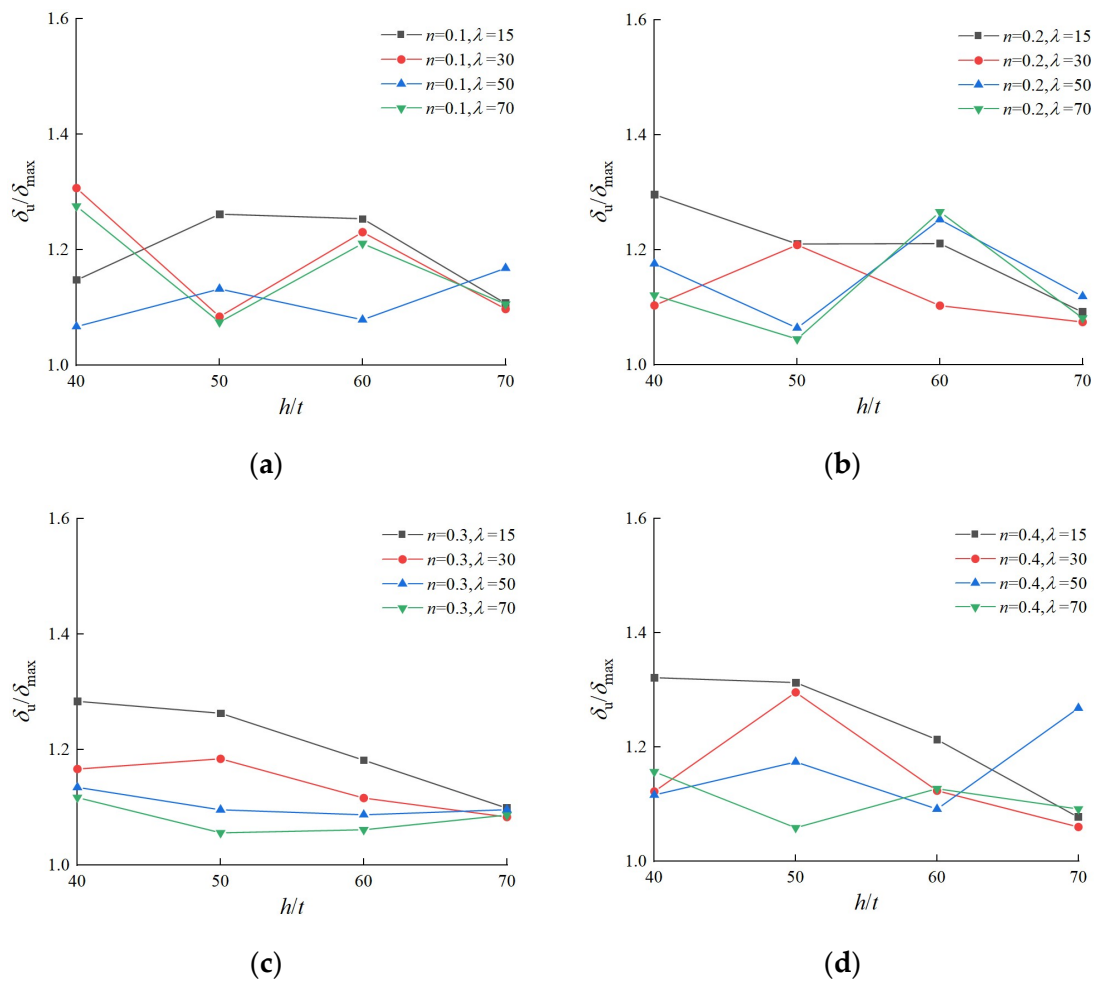


**Figure 22.** The effect of  $h/t$  on  $\delta_u/\delta_m$ . (a)  $n = 0.1$ ; (b)  $n = 0.2$ ; (c)  $n = 0.3$ ; (d)  $n = 0.4$ .

## 4.2. Simplify Restoring Force Model

### 4.2.1. Hysteresis Rules

Through the shape analysis of the hysteresis curve obtained by the FEA calculation, it is found that when the member is in the strengthening stage, the hysteresis loop of each level displacement is a parallelogram, and the unloading stiffness and elastic stiffness are almost the same. The unloading stiffness of the member is different under different buckling modes when the member is in the stiffness degradation stage. Through the analysis of the hysteretic behavior of the CFTWS lipped channel beam-column member, based on the determination of the characteristic point calculation formula of the skeleton curve model and the characteristics of the hysteresis curve in different buckling modes, the improved bilinear model is used to define the hysteresis rules of the beam-column members in different buckling modes:

#### 1. SRFM for CFTWS lipped channel members failed with strength or global buckling

The SRFM of a member that assumes that strength failure or global instability failure predominate is shown in Figure 23.

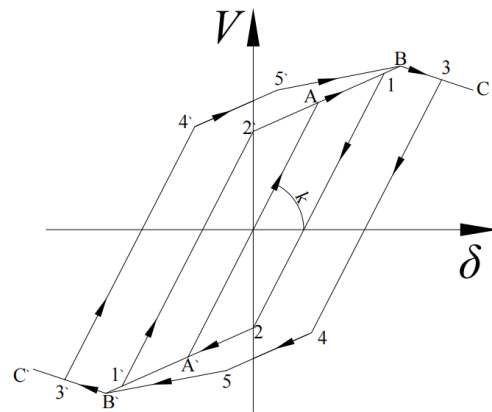


**Figure 23.** The SRFM for CFTWS lipped channel members failed with strength or global buckling.

The rules for the SRFM are assumed as follow:

When the load is unloaded from any point 1 (or 1') of the skeleton curve strengthening stage, its loading unload path is  $1 \rightarrow 2 \rightarrow A' \rightarrow 1' \rightarrow 2' \rightarrow A \rightarrow 1$ . When the load is unloaded from any point 3 (or 3') of the stiffness degradation stage of the skeleton curve, its loading unload path is  $3 \rightarrow 4 \rightarrow 5 \rightarrow B' \rightarrow 3' \rightarrow 4' \rightarrow 5' \rightarrow B \rightarrow 3$ . In the loading and unloading path, the unloading stiffness of segments 12 (1'2') and 34 (3'4') is the same as the initial stiffness of the skeleton curve, and their length is equal to that of the line segment AA. The unloading stiffness of segments 1'2', 2'1', 45 or 4'5' is equal to the initial stiffness on the skeleton curve, the absolute values of the abscissa of point 1 (2), 3(4) and 5 are equal to 1'(2'), 3'(4') and 5, respectively. The length of segments 45 and 4'5' is equal to the length of the AB (or A'B') segment on the skeleton curve.

## 2. SRFM model for CFTWS lipped channel members failed with local buckling

After the horizontal load at the top of the column exceeds the peak load, the unloading curve of the member is fixed at a fixed point. Therefore, the load-displacement SRFM of a member that assumes that local instability failure predominates is shown in Figure 24.

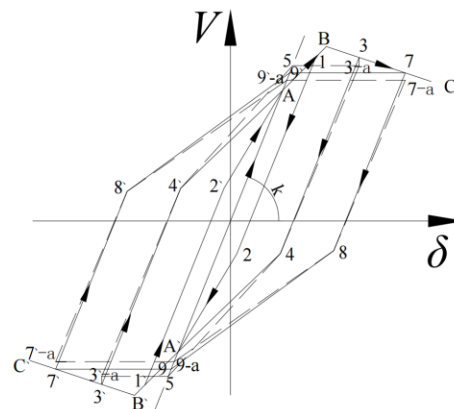


**Figure 24.** The SRFM for local instability failure.

Load unload rules for SRFM are assumed to be:

When the load is unloaded from any point 1 (or 1') of the skeleton curve strengthening stage, its loading unload path is  $1 \rightarrow 2 \rightarrow A' \rightarrow 1' \rightarrow 2' \rightarrow A \rightarrow 1$ . When the load is unloaded from any point 3 of the stiffness degradation stage of the skeleton curve, its loading unloading path is  $3 \rightarrow 4 \rightarrow A' \rightarrow B' \rightarrow 3' \rightarrow 4' \rightarrow A \rightarrow B \rightarrow 3$ . When unloaded on the second turn, its load unload path is  $3-a \rightarrow 4 \rightarrow 5 \rightarrow 3'-a \rightarrow 4' \rightarrow 5' \rightarrow 3-a$ . When the load is unloaded from any point 7 of the stiffness degradation stage of the skeleton curve, its loading unloading path is  $7 \rightarrow 8 \rightarrow 9 \rightarrow 7' \rightarrow 8' \rightarrow 9' \rightarrow 7$ ; When the second turn is unloaded, its load unload path



load values of point 1, point 3 ( $1'$ ,  $3'$ ), respectively. The load values at points 3-a ( $3'-a$ ) are 0.7 times the load values of point 3 ( $3'$ ), respectively. The load values at point 5 ( $5'$ ) are 0.9 times the load values of point 3 ( $3'$ ). Point 5, point  $5'$  located on the extension line of  $AA'$ , is located.

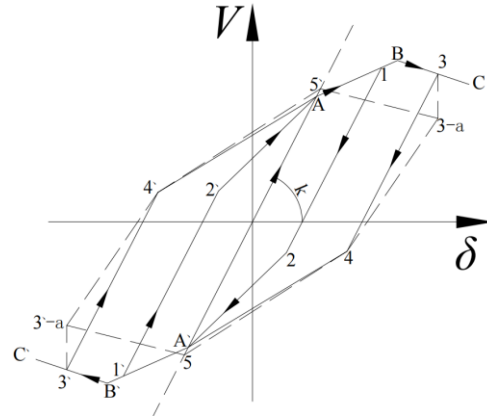


**Figure 26.** The SRFM for local and global coupling, distortional and global coupling destruction.

#### 4.2.2. Verification of Simplify Restoring Force Model

By comparing on the hysteresis curves between the proposed SRFM and the FEA results, the reliabilities of the proposed SRFM for CFTWS lipped channel members failed with different buckling modes can be verified.

1. The comparison on the hysteresis curves between the proposed SRFM and the FEA model for CFTWS lipped channel members failed with strength is shown in Figure 27.

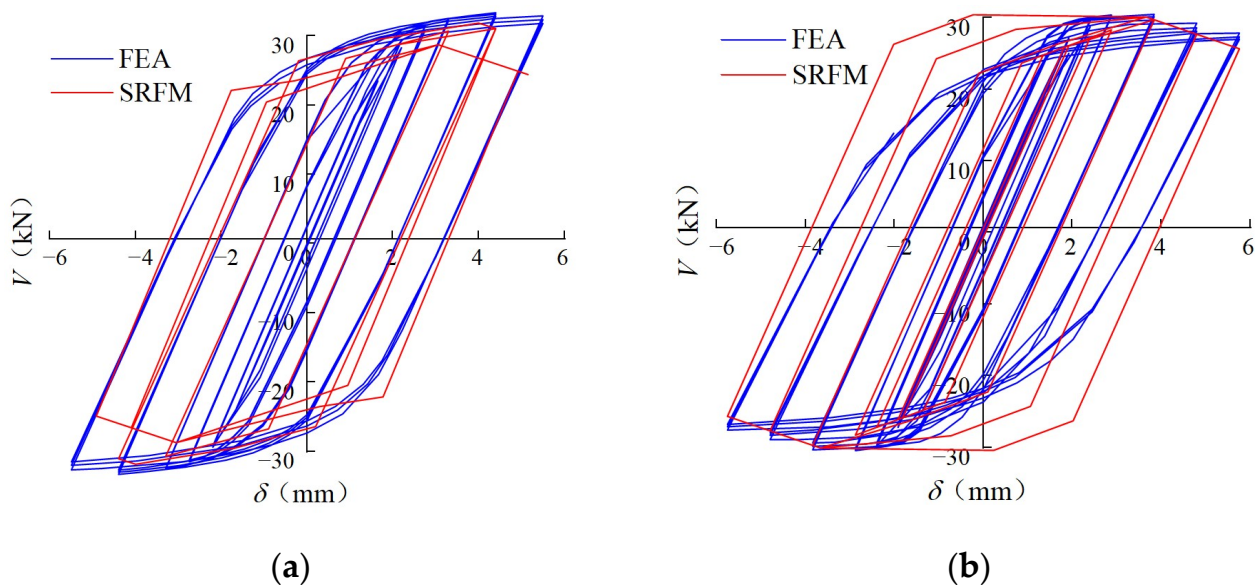


**Figure 27.** The comparison on the hysteresis curves between FEA model and SRFM for members failed with strength. (a) C1-BC-L15-40-02. (b) C1-BC-L15-40-03.

2. The comparison on the hysteresis curves between the proposed SRFM and the FEA model for CFTWS lipped channel members failed with global buckling is shown in Figure 28.

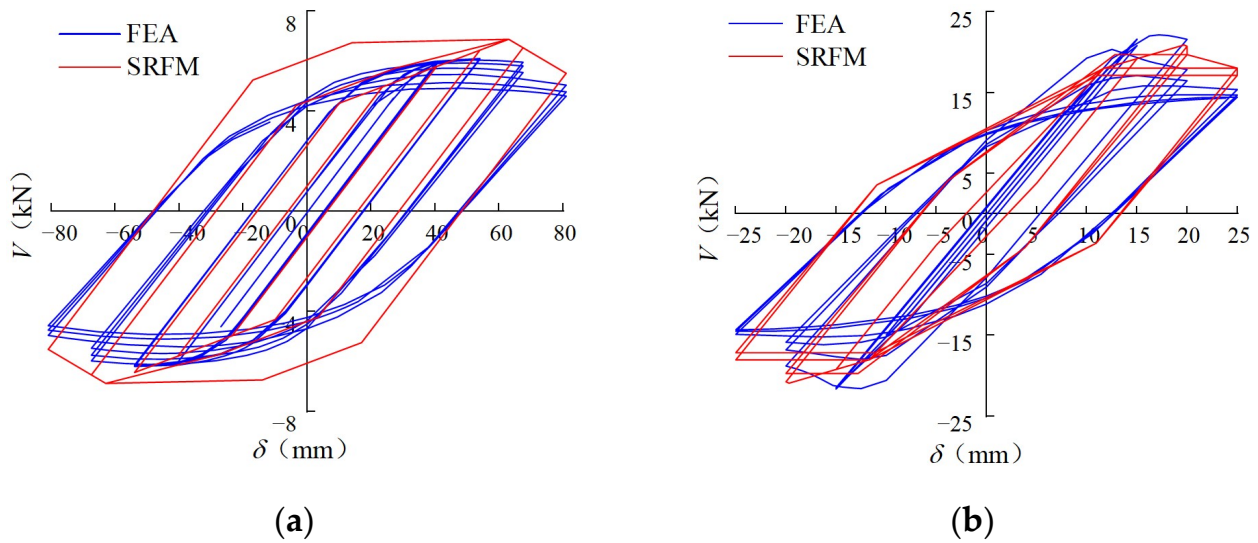


**Figure 28.** The comparison on the hysteresis curves between FEA model and SRFM for members failed with global buckling. (a) C1-BC-L70-40-01. (b) C2-BC-L50-50-01.

3. The comparison on the hysteresis curves between the proposed SRFM and the FEA model for CFTWS lipped channel members failed with local buckling is shown in Figure 29.

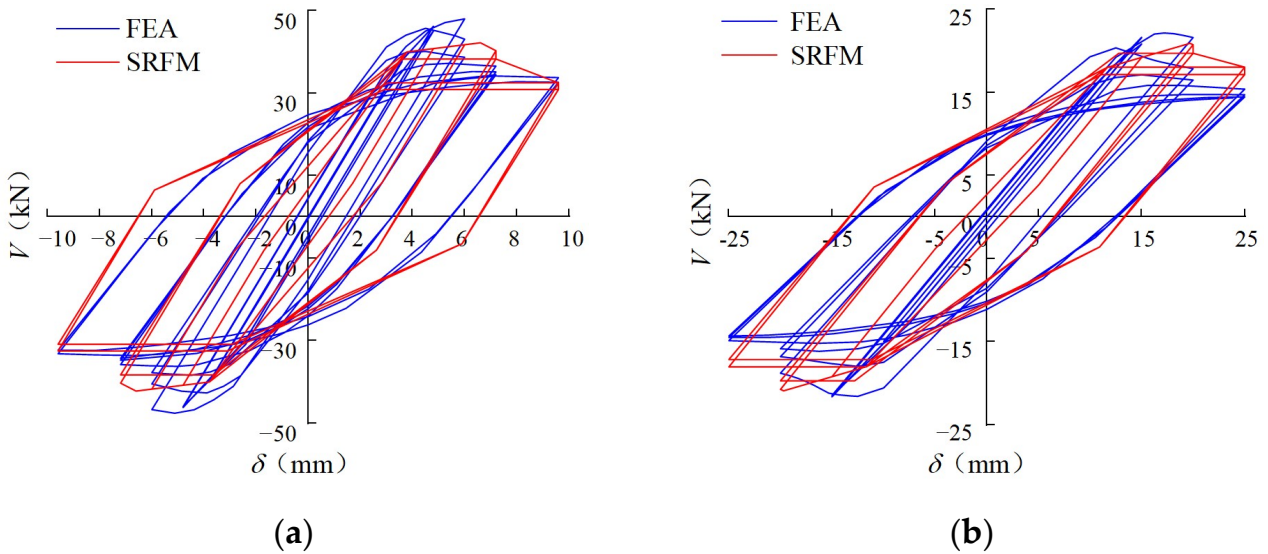


**Figure 29.** The comparison on the hysteresis curves between FEA model and SRFM for members failed with local buckling. (a) C4-BC-L15-70-02. (b) C4-BC-L30-70-02.

4. The comparison on the hysteresis curves between the proposed SRFM and the FEA model for CFTWS lipped channel members failed with distortional buckling is shown in Figure 30.

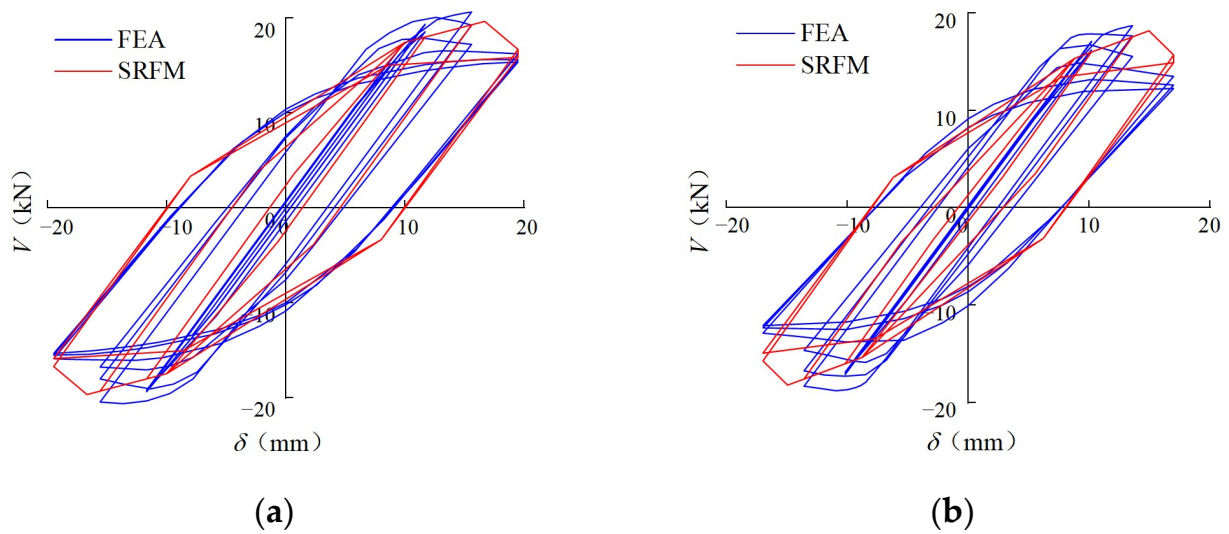


**Figure 30.** The comparison on the hysteresis curves between FEA model and SRFM for members failed with distortional buckling. (a) C3-BC-L30-60-02. (b) C3-BC-L30-60-03.

- The comparison on the hysteresis curves between the proposed SRFM and the FEA model for CFTWS lipped channel members failed with distortional and global coupling instability is shown in Figure 31.

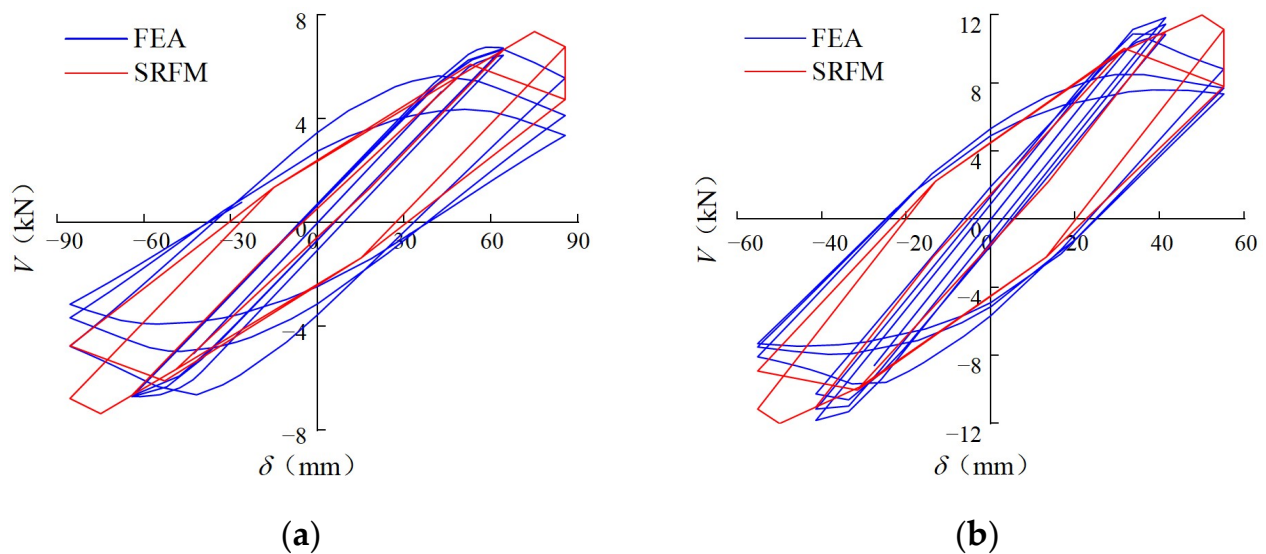


**Figure 31.** The comparison on the hysteresis curves between FEA model and SRFM for members failed with distortional and global coupling instability. (a) C3-BC-L70-60-02. (b) C4-BC-L50-70-02.

- The comparison on the hysteresis curves between the proposed SRFM and the FEA model for CFTWS lipped channel members failed with local and global coupling instability is shown in Figure 32.

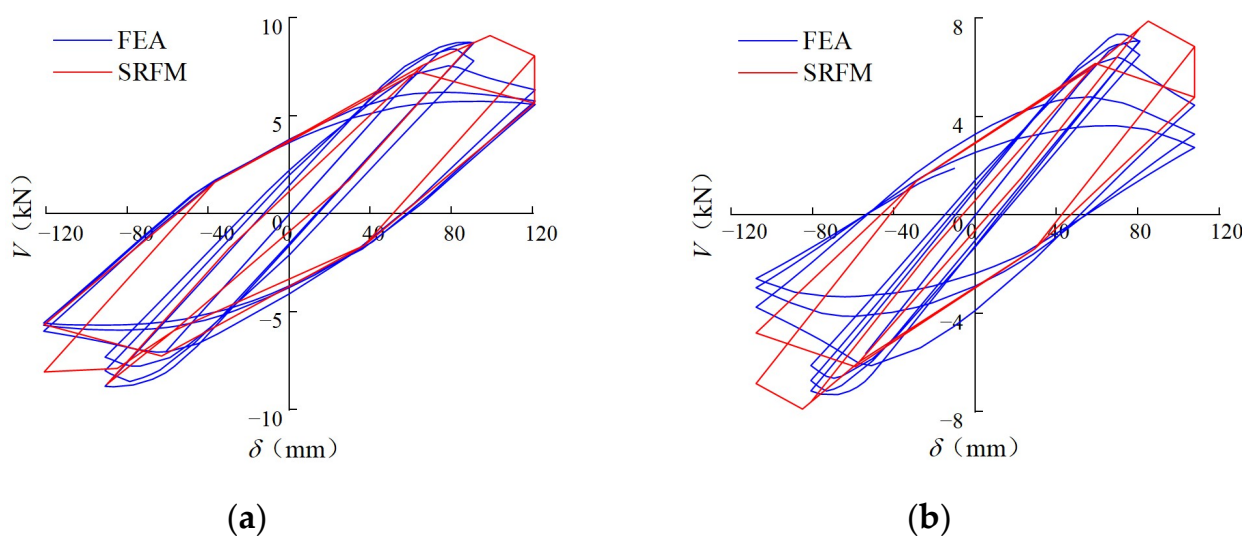


**Figure 32.** The comparison on the hysteresis curves between FEA model and SRFM for members failed with local and global coupling instability. (a) C4-BC-L70-70-01. (b) C4-BC-L70-70-02.

It can be seen from Figures 27–32 that the SRFM of the beam-column member in different buckling modes coincides well with the hysteresis curve of the member. The proposed SRFM can better reflect the basic characteristics of the hysteresis curve of the member. This SRFM is suitable for the CFTWS lipped channel beam-column members with the width-to-thickness ratio of 40~70, the slenderness ratio of 15~70, and the axial compression ratio of 0~0.4.

## 5. Conclusions

With 80 CFTWS lipped channel beam-column members with different the width-to-thickness ratios, the slenderness ratios and axial compression ratios were analyzed by using the finite element software. Based on the analyzed results, the hysteresis properties of the members under different buckling modes were studied and the SRFM of members under different buckling modes are proposed. The following conclusions are obtained:

- (1) The hysteresis characteristics of the CFTWS lipped channel beam-column members are mainly affected by the ratio of width-to-thickness, the slenderness ratio and axial compression ratio. The larger the slenderness ratio, the smaller the plastic moment that the member can withstand and the faster the stiffness degenerates. The ductility of the member decreases and the degradation of stiffness increases with the increase of the width-to-thickness ratio. With the increase of the axial compression ratio, the lower the ductility of the member decreases, the stiffness degradation increases, the plastic moment that can be tolerated is reduced and the energy consumption capacity is weakened.
- (2) According to the analysis on the influence of the width-to-thickness ratios, the slenderness ratios and axial compression ratios on the beam-column members, the failure modes of the CFTWS lipped channel beam-column members can be divided into six modes: strength failure, local buckling, distortional buckling, global buckling, interactive buckling of local buckling and global buckling, interactive buckling of distortional buckling and global buckling. CFTWS lipped channel beam-column members with the strength failure and local buckling show good seismic performance. The members with local buckling have a considerable local buckling reserve.
- (3) Based on the results of finite element parametric analysis, a skeleton curve model suitable for the CFTWS lipped channel beam-column members is proposed through data regression analysis. By analyzing the hysteresis curve of the FEA, the SRFM under different buckling modes are established. The comparisons on the hysteresis

curve between the FEA and proposed method show that the proposed SRFM can indicate greatly the characteristics of the hysteretic behavior of the CFTWS lipped channel beam-column member.

**Author Contributions:** Conceptualization, X.Y. and Y.G.; methodology, X.Y.; validation, Y.G.; investigation, Y.G. and Y.G.; data curation, J.Y.; writing—original draft preparation, J.Y.; writing—review and editing, J.Y. and X.Y.; funding acquisition, X.Y. All authors have read and agreed to the published version of the manuscript.

**Funding:** This research was funded by National Natural Science Foundation of China grant number [51868049].

**Data Availability Statement:** All the data included in this study are available upon request by contacting the corresponding author.

**Conflicts of Interest:** The authors declare no conflict of interest.

## References

1. Hancock, G.J.; Rasmussen, K.J.R. Recent research on thin-walled beam-columns. *Thin-Walled Struct.* **1998**, *32*, 3–18. [\[CrossRef\]](#)
2. Hancock, G.J. Cold-formed steel structures. *J Constr Steel Res.* **2003**, *59*, 473–487. [\[CrossRef\]](#)
3. Kumar, S.; Usami, T. An evolutionary-degrading hysteretic model for thin-walled steel structures. *Eng Struct.* **1996**, *18*, 504–514. [\[CrossRef\]](#)
4. Usami, T.; Ge, H.B. Cyclic behavior of thin-walled steel structures—Numerical analysis. *Thin-Walled struct.* **1998**, *32*, 41–80. [\[CrossRef\]](#)
5. Goggins, J.M.; Broderick, B.M.; Elghazouli, A.Y.; Lucas, A.S. Experimental cyclic response of cold-formed hollow steel bracing members. *Eng Struct.* **2005**, *27*, 977–989. [\[CrossRef\]](#)
6. Goggins, J.M.; Broderick, B.M.; Elghazouli, A.Y.; Lucas, A.S. Behaviour of tubular steel members under cyclic axial loading. *J. Constr. Steel Res.* **2006**, *62*, 121–131. [\[CrossRef\]](#)
7. Yang, N.; Zhong, Y.N.; Meng, Q.T.; Zhang, H. Hysteretic behaviors of cold-formed steel beam-columns with hollow rectangular section: Experimental and numerical simulations. *Thin-Walled Struct.* **2014**, *80*, 217–230. [\[CrossRef\]](#)
8. Padilla-Llano, D.A.; Moen, C.D.; Eatherton, M.R. Cyclic axial response and energy dissipation of cold-formed steel framing members. *Thin-Walled Struct.* **2014**, *78*, 95–107. [\[CrossRef\]](#)
9. Padilla-Llano, D.A.; Eatherton, M.R.; Moen, C.D. Cyclic flexural response and energy dissipation of cold-formed steel framing members. *Thin-Walled Struct.* **2016**, *98*, 518–532. [\[CrossRef\]](#)
10. Li, G.W.; Li, Y.Q.; Ji, H.; Li, T.; Zheng, J. Investigation on the hysteretic behavior of axially loaded cold-formed thick-walled steel members. *Structures* **2022**, *38*, 1411–1425. [\[CrossRef\]](#)
11. Jiang, L.Z.; Goto, Y.; Obata, M. Hysteretic modeling of thin-walled circular steel columns under biaxial bending. *J. Struct. Eng.* **2002**, *128*, 319–327. [\[CrossRef\]](#)
12. Shen, Z.Y.; Wen, D.H.; Li, Y.Q.; Ma, Y.F. Distribution Patterns of Material Properties for Cross-section of Cold-formed Thick-walled Steel Rectangular Tubes. *J. Tongji Univ.* **2016**, *44*, 981–990. (In Chinese)
13. Wen, D.H. *Research on Seismic Behavior of Cold-Formed Thick-Wall Steel Beam-Column Members*; Tongji University: Shanghai, China, 2014.
14. Fu, X.C.; Li, Y.Q.; Shen, Z.Y. Research on the seismic behaviors of opening cold-formed thick-walled steel under the axial cyclic loading. *J. Hebei Univ. Eng.* **2016**, *33*, 1–7. (In Chinese)
15. Fu, X.C. *Research on the Seismic Performance of Open-Section Cold-Formed Thick-Walled Steel Members*; Tongji University: Shanghai, China, 2016.
16. Chen, L.C.; Cheng, X.; Chen, Y.Y. Research on restoring force model of H-section steel members under uniaxial compression and bending considering local buckling. *Eng. Mech.* **2021**, *38*, 80–92. (In Chinese)
17. Yang, N.; Peng, X. Research on hysteretic model and buckling mechanism of cold-formed C-section steel column. *China Civ. Eng. J.* **2015**, *48*, 25–33. (In Chinese)
18. Yang, N.; Peng, X.; Yang, Q.S. Analysis of hysteretic performance of C-section specimens of cold-formed steel. *J. Civ. Archit. Environ. Eng.* **2012**, *34*, 69–76. (In Chinese)
19. Liu, Z.Q.; Du, Z.Y.; Xue, J.Y.; Zhou, C.F. Study on damage-based restoring force model of steel reinforced concrete special-shaped columns. *Eng. Mech.* **2022**, 36–147.
20. Wang, T.; Jiang, R.N.; Yuan, S.F.; Yuan, K.; Li, L.W.; Zhou, G.Y. A Restoring Force Model for Prefabricated Concrete Shear Walls with Built-In Steel Sections. *Appl. Sci.* **2021**, *11*, 12131. [\[CrossRef\]](#)
21. Zhao, J.; Dun, H.H. A restoring force model for steel fiber reinforced concrete shear walls. *Eng. Struct.* **2014**, *75*, 469–476. [\[CrossRef\]](#)
22. Wu, C.L.; Liu, X.; Pan, W.; Mou, B. Restoring force model for modular prefabricated steel-reinforced concrete column to H-shaped steel beam composite joints. *J. Build. Eng.* **2021**, *42*, 102845. [\[CrossRef\]](#)

23. Zhang, J.W.; Zheng, W.B.; Cao, W.L.; Dong, H.Y.; Li, W.D. Seismic behavior of low-rise concrete shear wall with single layer of web reinforcement and inclined rebars: Restoring force model. *KSCE J. Civ. Eng.* **2019**, *23*, 1302–1319. [[CrossRef](#)]
24. Chen, Y.; Chen, C.; Chen, C. Study on seismic performance of prefabricated self-centering beam to column rotation friction energy dissipation connection. *Eng. Struct.* **2021**, *241*, 112136.
25. Liu, J.C.; Tian, L.; Ma, R.S.; Qu, B. Development of a hysteretic model for steel members under cyclic axial loading. *J. Build. Eng.* **2022**, *46*, 103798. [[CrossRef](#)]
26. Lam, S.S.E.; Chung, K.; Wang, X. Load-carrying capacities of cold-formed steel cut stub columns with lipped C-section. *Thin-Walled Struct.* **2006**, *44*, 1077–1083. [[CrossRef](#)]
27. Yang, J.; Guo, Y.; Yu, L.; Hu, C.; Liu, Y. Research on Hysteretic Behavior of Cold-Formed Thin-Wall Rolled Edge Channel Steel Flexural Members. *J. Phys. Conf. Ser.* **2022**, *2185*, 012066. [[CrossRef](#)]
28. Contento, A.; Aloisio, A.; Xue, J.; Quaranta, G.; Briseghella, B.; Gardoni, P. Probabilistic axial capacity model for concrete-filled steel tubes accounting for load eccentricity and debonding. *Eng. Struct.* **2022**, *268*, 114730. [[CrossRef](#)]
29. Peterman, K.D.; Nakata, N.; Schafer, B.W. Hysteretic characterization of cold-formed steel stud-to-sheathing connections. *J. Constr. Steel Res.* **2014**, *101*, 254–264. [[CrossRef](#)]
30. Nithyadharan, M.; Kalyanaraman, V. Modelling hysteretic behaviour of cold-formed steel wall panels. *Eng. Struct.* **2013**, *46*, 643–652. [[CrossRef](#)]
31. Xu, Z.; Du, Q.; Chen, Z.; Chen, H. Hysteretic behavior of cold-formed steel reinforced concrete shear walls with steel meshes. *J. Constr. Steel Res.* **2022**, *197*, 107445. [[CrossRef](#)]
32. Tong, G.S. *In-Plane Stability of Steel Structure*; China building industry press: Beijing, China, 2005.

**Disclaimer/Publisher’s Note:** The statements, opinions and data contained in all publications are solely those of the individual author(s) and contributor(s) and not of MDPI and/or the editor(s). MDPI and/or the editor(s) disclaim responsibility for any injury to people or property resulting from any ideas, methods, instructions or products referred to in the content.